Chinese Journal of Aeronautics, (2019), 32(3): 701–714

Chinese Society of Aeronautics and Astronautics
& Beihang University

Chinese Journal of Aeronautics

cja@buaa.edu.cn
www.sciencedirect.com

# Effect of selective laser treatment on initiation of fatigue crack in the main part of an undercarriage drag strut

**Anna BIEŃ [a], Marek SZKODO [b,*], Jerzy DOBERSKI [c], Bartłomiej KARPIŃSKI [b]**

[a] *Technical Sciences Faculty, University of Warmia and Mazury in Olsztyn, Oczapowskiego 11, 10-719 Olsztyn, Poland*
[b] *Mechanical Engineering Faculty, Gdansk University of Technology, Narutowicza 11/12, 80-233 Gdańsk, Poland*
[c] *Military Aircraft Factory No. 2 Joint Stock Company, Szubińska 107, 85-915 Bydgoszcz, Poland*

Received 10 November 2017; revised 20 December 2017; accepted 2 February 2018
Available online 21 June 2018

**KEYWORDS**

Fatigue wear;
Laser re-melting;
Nanoindentation testing;
Residual stresses;
Steel alloy

**Abstract** This paper presents the results of material characterization and a fatigue test conducted for a laser-re-melted drag strut used in an aircraft landing gear. The drag strut was re-melted with a $CO_2$ laser beam. Eight re-melted paths were made in the form of spiral lines along the axis of the drag strut. Next, the drag strut was subjected to variable loads on a testing machine simulating loads occurring when an aircraft lands. The fatigue test showed that the laser-treated drag strut was able to withstand 1700 simulated cycles of landing. This result was 70% better than that obtained for a drag strut with no laser treatment. In order to find the reason for the increase in the number of cycles of simulated landings, tests were carried out using transmission and scanning electron microscopes, a computer microtomograph, an X-ray diffractometer, and a nanoindenter, respectively. Results of the conducted research indicated that the reasons for the increased fatigue life of the laser-treated undercarriage drag strut were both an ultra-fine cellular martensitic microstructure and compressing residual stresses generated during the laser re-melting of the surface layer of the material.


## 1. Introduction

Laser beam has been used in surface engineering for more than half a century. Laser surface treatment is used for enhancing the surface properties of components for example to increase the cavitation erosion resistance.[1,2] In addition, laser beam has been used to increase the fatigue resistance of various types of materials.[3–7] Therefore, many examples can be found in the

* Corresponding author.
E-mail address: mszkodo@pg.gda.pl (M. SZKODO).
Peer review under responsibility of Editorial Committee of CJA.

Production and hosting by Elsevier

https://doi.org/10.1016/j.cja.2018.05.021

literature describing the use of laser processing to increase the service lives of aircraft components.[8–13]

Many authors noticed[14–23] that laser treatment is able to induce a treated surface layer with beneficial compressive residual stresses which contribute to increasing the fatigue resistance. For example, Grum and Slabe[24] utilized laser-re-melting of maraging steel to repair fatigued surfaces of parts made of this steel, where the presence of surface microcracks may be observed. They have shown that for 320 J/mm$^2$ energy density laser beam, there are compressive residual stresses in treated steel reaching a value of 0.45 GPa. Meanwhile, Yang et al.[25] reported that laser re-melting of the train track alloy steel increases its rolling contact fatigue wear resistance. They concluded that better potential on the rolling contact fatigue wear resistance is related to the microhardness, microstructure, and stress concentration after laser treatment. In turn, Gerritsen et al. concluded in their work[26] that the laser re-melting process of two high-strength steel grades, S690QL and S960QL, causes a 40% increase in fatigue strength due to reduction of tensile stresses caused by welding.

Laser processing of alloys changes their microstructures, which also affects the fatigue properties of the processed material. For example, Lavvafi et al.[27] have shown improvements in the fatigue behaviour of laser-treated 316LVM biomedical grade wires. They concluded that low-power Nd:YAG laser-treated AISI 316LVM annealed wires exhibited better fatigue performance in both high- and low-cycle fatigue compared to that of as-received AISI 316LVM annealed wires. The improved or decreased fatigue behaviour was related to laser machining effect on a number of different factors that included defect generation and microstructural refinement. It was not clear what levels of residual stress were being generated. In our previous papers,[28–30] we have also shown relationships between microstructures of laser treated steels and their fatigue properties. For example, in low-alloy steel with a content of 0.30% C, laser re-melting of treated surface just in front of a fatigue crack can stop it. Research conducted on round compact tensile (RCT) specimens made of steel alloy containing chrome, manganese, silicon, and nickel (30HGSNA) re-melted by laser showed more than a 30-fold increase of the fatigue strength.[29] As far as the microstructure is concerned, it has been demonstrated that the blockage of a fatigue fracture is due to the change of the microstructure of the laser-processed path and its location relative to the initiated fracture.[30] Moreover, multiple laser re-melting of carbon steel results in a high density of crystallographic defects in a martensite[31] which, in turn, generates an increase of the fatigue strength.

However, laser re-melting can also contribute to the deterioration of the state surface, and in addition, it can cause cracks and porosity in the processed microstructure[32] thus to a reduction of the fatigue resistance of the workpiece.

The aim of the work is to present the possibility of performing laser treatment of an undercarriage drag strut, by selective re-melting of its surface, in order to increase its fatigue life. This work contributes to understanding the reasons for increasing the fatigue resistances of laser re-melted metallic structures. The work focuses on initiating high-cycle fatigue (HCF) cracks at inclusions in a high-strength martensitic steel after its laser re-melting, and on the description of the influences of both the microstructure and residual stress on the development of fatigue cracks.

## 2. Experimental procedure

### 2.1. Object of investigation

One drag strut was used for testing. Fig. 1 shows the shape and dimensions of the drag strut, where 1 – pipe; 2 – retaining ring; 3 – tip; 25′A – fit designation (a means deviation value on +0.023), designation a 6.3-joint thickness 6.3 mm. The drag strut was made of a low-alloy steel with a content of 0.30% C. The chemical composition of the steel is presented

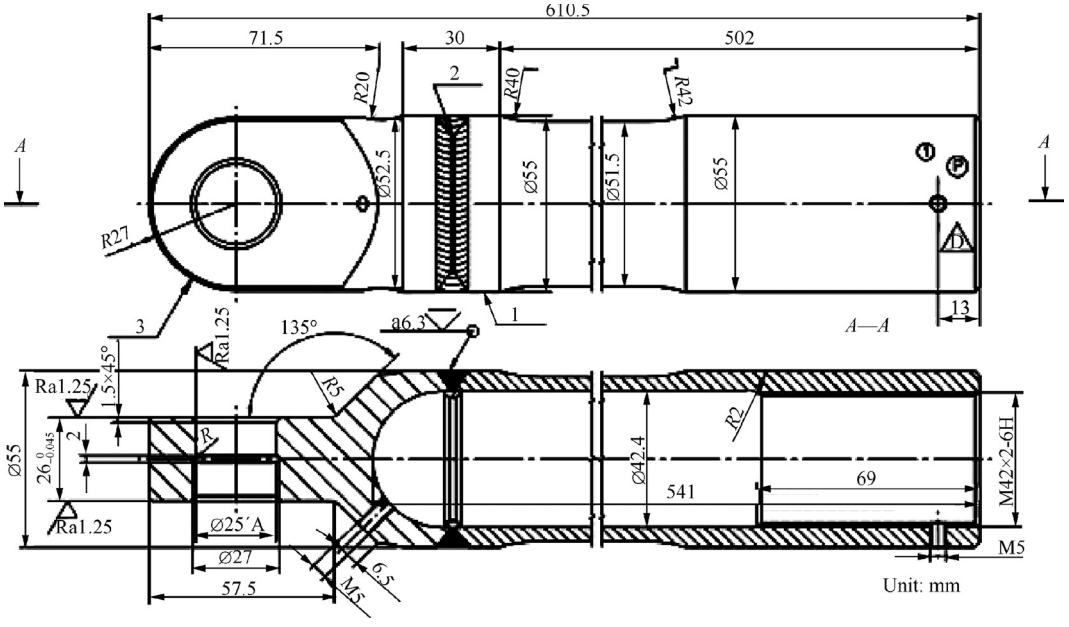


**Fig. 1** Shape and dimensions of the drag strut used for testing.

**Table 1** Chemical composition of the steel used to make the drag strut.

| Element | C | Mn | Si | P | S | Cu | Cr | Ni |
|---|---|---|---|---|---|---|---|---|
| Content (wt%) | 0.30 | 1.15 | 1.10 | 0.030 | 0.025 | 0.25 | 1.05 | 1.65 |

in Table 1. This steel is designed for quenching and tempering, and it is designated for parts of machines and engines subjected to the highest loads, thus requiring very good plastic properties. This grade of steel is used, among others, in the aircraft industry.

The drag strut was subjected to the following heat treatment: isothermal hardening from 900 °C and double tempering, first at a temperature of 280 °C/3 h and second at 270 °C/3 h. After tempering, the drag strut was cooled in air. Mechanical properties of the steel after heat treatment are listed in Table 2. Then, the surface of the drag strut underwent phosphatising. After this process, iron phosphates were formed on the surface of the drag strut. Phosphate coating thickness ranges from 2 μm to 3 μm.

### 2.2. Laser beam treatment

Next, the drag strut was subjected to laser treatment. Laser surface processing of the drag strut sleeve was designed on the basis of the conclusions of our previous studies,[23,30] which describe and explain the phenomenon of blocking fatigue crack propagation (obtained using laser technology for steel of the same species, hardened and tempered to a hardness of 50 HRC). Because the phosphated surface of the drag strut, laser treatment was performed with no laser beam absorbent. The guideline for the design of the melted paths trajectory – spiral with a pitch equal to the sleeve length of the drag strut was that cracks formed in the area of the sleeve of the drag strut were disposed perpendicularly to the axis of the sleeve. In order to reduce torsional stresses in the sleeve of the processed drag strut, an alternating direction of performed pathways was used. With this technique, eight melted paths were made as spiral lines along the axis of the drag strut (see Fig. 2). The laser processing parameters for treatment of the drag strut are presented in Table 3. Fig. 2 shows a schematic drawing of the section of the re-melted undercarriage drag strut with a single re-melted path marked in Fig. 2(a), and the arrangement of re-melted paths on the perimeter in Fig. 2(b). The amount of energy delivered by the laser beam to the workpiece was selected on the basis of earlier experiments by optimizing the thickness of the re-melted layer.

**Table 2** Mechanical properties of the steel used to make the drag strut.

| Mechanical property | Value |
|---|---|
| Tensile strength | 1620 MPa |
| Hardness | 46.5–50.5 HRC |
| Yield strength | 1510 MPa |
| Elongation | 10% |
| Reduction of area | 45% |
| Toughness | 48 J |

### 2.3. Fatigue test

After laser processing, a fatigue test of the laser treated drag strut was performed. The fatigue test was performed on a testing machine MTS 8502 (Instron) at the Air Force Institute of Technology in Warsaw. The MTS 8502 was equipped with a head of a force range of ±250 kN. The instantaneous values

**Table 3** Laser parameters used for melting of the sample.

| Parameter | Value |
|---|---|
| Laser type | $CO_2$ |
| Laser mode | Pulse $TEM_{10}$ |
| Laser average power | $P$ = 860–900 W |
| Radius spot laser (the conversion) | $r$ = 2 mm |
| The speed of the laser beam | $v$ = 3.5–4.5 mm/s |
| Shielding gas (low-pressure) | Argon 5.0 |
| Distance of the sample from the plane of beam focusing lens | 120 mm |
| Focal length of lens | 3.8 inch |

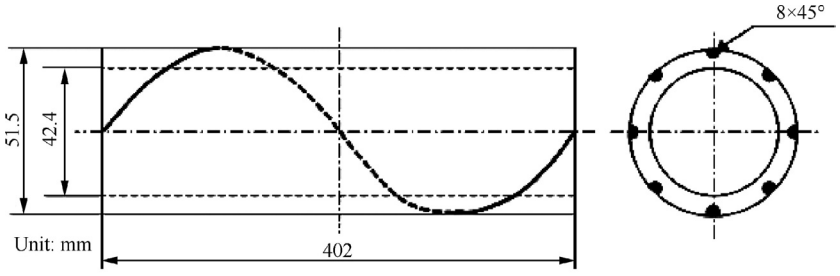


(a) Section of re-melted undercarriage (b) Arrangement of re-melted paths on perimeter

**Fig. 2** Eight melted paths were made as spiral lines along the axis of the drag strut.

**Table 4** Parameters used for the fatigue test of the drag strut of landing gear.

| Stage number | Number of cycles per stage | Maximum load $P_{max}$ (kN) | Stress ratio $R = \sigma_{min}/\sigma_{max}$ | Stage number | Number of cycles per stage | Maximum load $P_{max}$ (kN) | Stress ratio $R = \sigma_{min}/\sigma_{max}$ |
|---|---|---|---|---|---|---|---|
| 1 | 3 | 9.77 | 0 | 17 | 2 | 195.4 | 0 |
| 2 | 18 | 19.54 | 0 | 18 | 10 | −19.4 | $-\infty$ |
| 3 | 25 | 29.34 | 0 | 19 | 60 | −9.77 | $-\infty$ |
| 4 | 44 | 39.08 | 0 | 20 | 5 | 9.77 | 0 |
| 5 | 5 | 48.85 | 0 | 21 | 2 | 19.54 | 0 |
| 6 | 9 | 68.39 | 0 | 22 | 5 | 29.31 | 0 |
| 7 | 2 | 97.7 | 0 | 23 | 2 | 39.08 | 0 |
| 8 | 13 | 107.47 | 0 | 24 | 5 | 48.85 | 0 |
| 9 | 1 | 117.24 | 0 | 25 | 9 | 68.39 | 0 |
| 10 | 7 | 127.01 | 0 | 26 | 15 | 97.7 | 0 |
| 11 | 43 | 136.78 | 0 | 27 | 35 | 107.47 | 0 |
| 12 | 30 | 146.55 | 0 | 28 | 40 | 117.24 | 0 |
| 13 | 100 | 156.32 | 0 | 29 | 60 | 127.01 | 0 |
| 14 | 110 | 166.09 | 0 | 30 | 200 | 136.78 | 0 |
| 15 | 40 | 175.86 | 0 | 31 | 25 | 146.55 | 0 |
| 16 | 20 | 185.63 | 0 | 32 | 5 | 156.32 | 0 |

of loading force and elongation of the drag strut were recorded during the fatigue test. One set of loads, consisting of 950 different cycles, represented all loads during one aircraft landing and taking off. 32 stages of loads occurred in one set of loads. The maximum magnitude of the force in each set of loads was $F = 195.4$ kN, and the minimum was $F = -19.54$ kN. The maximum loads and their numbers in a certain stage of the set of loads are shown in Table 4. A graphical form of one program of the set of loads is shown in Fig. 3 as the $n_i$ number of cycles at the $i$-th level of loads. The rate of the change of loadings was constant during the fatigue test, and it was 200 kN/s. The duration of one program of the set of loads was 18.56 min. The temperature during the test ranged between 20 and 25 °C, and the air humidity was 40–60%. The drag strut was tested by axial cycling in a laboratory environment at stress ratios $R$ from 0 to $-\infty$ (the minimum stress to the maximum stress). The stress ratio $R$ was 0 for 880 cycles, and $-\infty$ for 70 cycles in each stage. The load frequency was 0.85 Hz. On one end, the drag strut was fixed in the testing machine by the eyelet of the drag strut, and on the other end by the eye bolt screwed into the drag strut (see Fig. 4).

### 2.4. Material characterization

The microstructures of the steel before and after laser re-melting were examined by an X-ray diffractometer

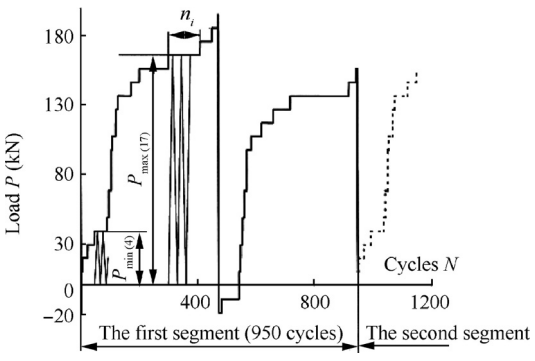


**Fig. 3** Set of loads program occurred during the fatigue test.

**Fig. 4** Stand for the fatigue test.

(XRD, with Cu Kα radiation $\lambda = 0.15418$ nm), a scanning electron microscope (SEM, JOEL JSM-7800F) equipped with X-ray energy-dispersive spectroscopy (EDS), a transmission electron microscope, a CT-scanner (phoenix v/tome/x s 240 kV), and a non-contact, optical, three-dimensional device based on focus-variation (Alicona 3D viewer), respectively. An Alicona 3D viewer enables fully automatic surface roughness measurements with both profile- and area-based parameters. The setting parameters of the Alicona 3D viewer used for the topography measurement of the laser post-processed drag strut are presented in Table 5. Metallographic investigations were carried out on parts of the sample within the melted zone, in the heat affected zone, and in the raw material. A sample was taken from a distance of about 15 cm from the fatigue fracture. The sample was grinded and polished to obtain an ultra-smooth surface before metallographic examination. An EDS analysis was performed in order to identify the precipitates in the microstructure. Transmission electron microscopy was also used for metallographic examination.

Metallographic observations were carried out using thin films. Microscopic examination was performed at an accelerating voltage of 45 kV.

**Table 5** Setting parameters used for the topography measurement.

| Parameter | Value |
|---|---|
| Objective magnification | 10× |
| Working distance | 17.5 mm |
| Lateral measurement range ($X,Y$) | 2 mm |
| $XY$ | 4 mm$^2$ |
| Vertical resolution | 100 nm |
| Height step accuracy (1 mm) | 0.05% |
| Maximal measurable area | 2500 mm$^2$ |
| Minimum measurable roughness ($R_a$) | 0.3 μm |
| Minimum measurable roughness ($S_a$) | 0.15 μm |
| Minimum measurable radius | 5 μm |

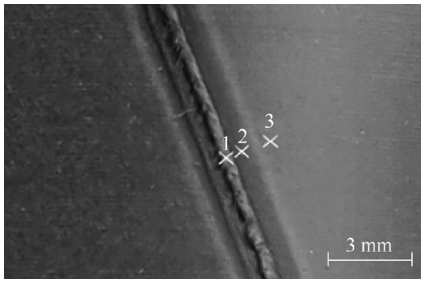


**Fig. 5** Drag strut surface with re-melted paths, heat affected zones, and the raw material.

#### 2.4.1. Hardness and residual stress measurements

Hardness tests of the material were performed after the fatigue investigation, using a NanoTest Vantage nanoindenter. This test was performed to determine the quantitative residual stresses in the melted paths, in the heat-affected zones (HAZ), and in the unprocessed material. Residual stresses were measured, respectively, on the surface and on the cross section of the drag strut for the same sample as used for metallographic investigation. On the cross section, hardness tests were made along three sections, normal to the surface at distances from the surface ranging from 15 μm to 915 μm. 10 measurements placed every 100 μm were taken in each section. One section along which the hardness was measured passed through the center of the melted path, the second section passed through the center of the HAZ, and the third only through the raw material at a distance of 0.5 mm from the HAZ. Hardness tests on the cross section were performed with a constant depth of indenter penetration equal to 1450 nm. A Berkovitch indenter was used for the hardness investigations. Loading and unloading rates were 50 mN/s. Indentation contains one cycle with 5 s dwell at the maximum load. Quantitatively, residual stresses were determined by a method described in Ref.[33] For this purpose, after the hardness tests, the sample was subjected to stress relief annealing at 270 °C for 2 h. Annealing was performed in a vacuum furnace. Hardness tests were performed again after annealing, near the same measurement points as before annealing. Residual stresses were calculated as the difference between the penetrator load for the sample with and without stress, i.e., before and after annealing respectively, at the same depth of penetrator displacement, referred to the surface contact of the indentation ($\sigma_{res}$ $(P^* - P)/A$, where $P^*$ is the load for the same displacement of the indenter in the stressed material, $P$ the load for the same displacement of the indenter in the annealed material, and $A$ the contact area of the indentation). To obtain the residual stresses profiles from the surface up to 15 μm deep into the material, a multiple-load cycle with an increasing-load experiment was also done using a nanoindenter NanoTest Vantage. The minimum load was 100 mN, and the maximum load was 20 N. Loading and unloading rates were 50 mN/s. Indentation contains 10 cycles with 5 s dwell at the maximum load. Fig. 5 shows where the measurements were taken. Three points of hardness measurements are marked. In this case, hardness measurements were also made before and after annealing.

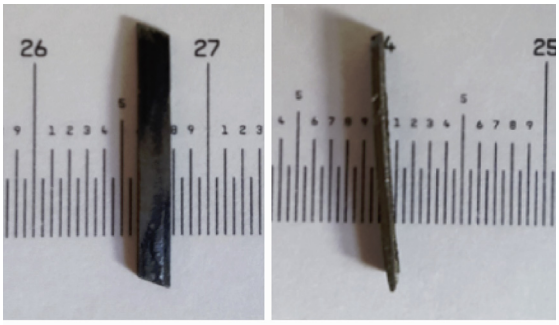


(a) Front view (b) Side view

**Fig. 6** Sample used to detect fatigue cracks initiation.

#### 2.4.2. Computed tomography measurement

To quantify the locations of fatigue cracks initiation, a sample with a size of 0.526 mm × 2 mm × 14.64 mm (see Fig. 6) was scanned using a Phoenix v|tome|x s240 X-ray computed scanner. The sample included both the melted material in the heat affected zone and the raw material. The sample was taken from a distance of about 10 cm from the fatigue fracture.

The v|tome|x s was equipped with both a 180 kV/15 W high-power nanofocus X-ray tube and a 240 kV/320 W microfocus tube. Scan data was reconstructed by the implementation of a graphics processing unit (GPU). The reconstructed data was then compiled on an HP z800 or z820 workstation. The data was collected and processed using Phoenix datos/x 2 acq software, but for the reconstruction, Phoenix datos/x 2 rec was used. The setting parameters of the CT scanner used for the measurement of the number of voids caused by fatigue loading are presented in Table 6.

**Table 6** Scanner setting parameters.

| Parameter | Value |
|---|---|
| Accelerating voltage | 80 kV |
| Current | 20 μA |
| Voxel size | 2.136 μm |
| Magnification | 93.64 |
| Number of images | 1400 |
| Exposure time | 1000 ms |
| Radiation filter | 0.2 mm Cu |

### 3. Results and discussion

Fig. 7 presents a view of the drag strut after the fatigue test. The fracture in the drag strut occurred in its main part, about 15 cm from the butt weld, joining the main part of the drag strut with the eyelet of the drag strut. The laser re-melted drag strut was able to withstand 1700 simulated cycles of landing. In contrast to the drag strut with no laser re-melting, the fracture in this drag strut occurred in the butt weld. It follows that the laser treatment can increase, for the same loading, the number of cycles to failure of the drag strut by about 70%. Subsequently, metallographic research was performed in order to verify the microstructural changes caused by the laser treatment. For this purpose, a sample was cut from the laser re-melted drag strut. The location of the cut corresponded to the spot of fracture in the drag strut with no laser re-melting. Then, a metallographic cross section was made. Structural examination of the cross section revealed that the laser treatment led to re-melting the surface layer to a depth of about 70 μm.

Fig. 8 shows two zones revealed in the re-melted area. The first zone covers an area up to about 15 μm from the surface. The microstructure of this zone is ultra-fine. Below the zone of highly-refined microstructure, there is a zone built of elongated dendrites in the direction of the largest heat dissipation in zone II (see Fig. 8(a)). The width of dendrites is about 1 μm. Dendritic axes coincide with the direction of the highest heat dissipation rate during the laser treatment, and they are perpendicular to the direction of fatigue loads. A heat-affected zone is located under the re-melted material zone. As demonstrated by X-ray studies, the microstructure consists of martensite, austenite, and iron phosphate (Fig. 9). The greater half-width of the main peak of martensite in re-melted "Zone I" (for a $2\theta$ angle of 44.85°) indicates a strong microstructure refinement. The half-width of the martensite peak in "Zone I" is 0.86°, and for martensite in the raw material, only 0.44°. The microstructure of this zone consists of martensite and retained austenite.

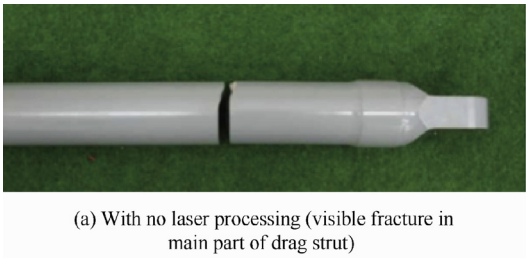

(a) With no laser processing (visible fracture in main part of drag strut)

(b) With re-melted paths (visible fracture in butt weld joining main part of drag strut and eyelet)

**Fig. 7** Two drag struts of landing gear after testing fatigue.

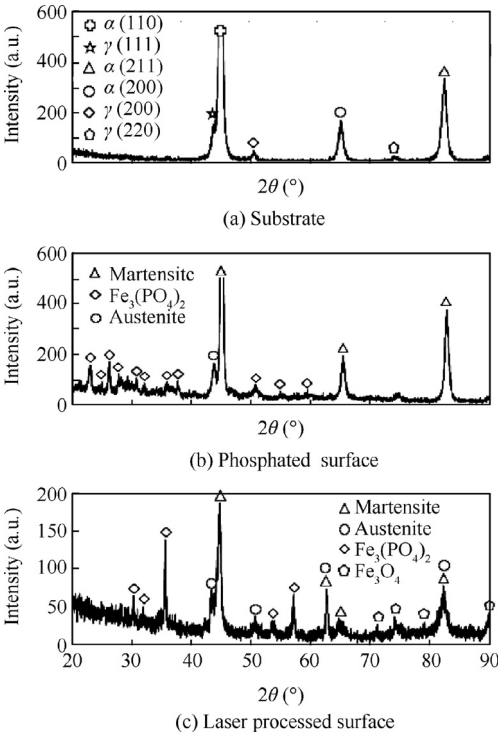


**Fig. 9** X-ray diffraction patterns of the substrate, phosphated surface, and laser-processed surface.

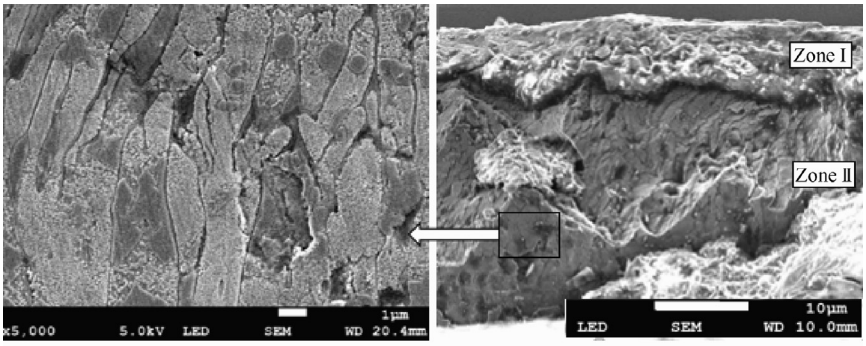


(a) Elongated dendrites in the direction of the largest heat dissipation in the zone II

(b) Ultra-fine microstructure in the zone I and dendritic structure in zone II

**Fig. 8** SEM breakthrough of the area melted by a laser beam.

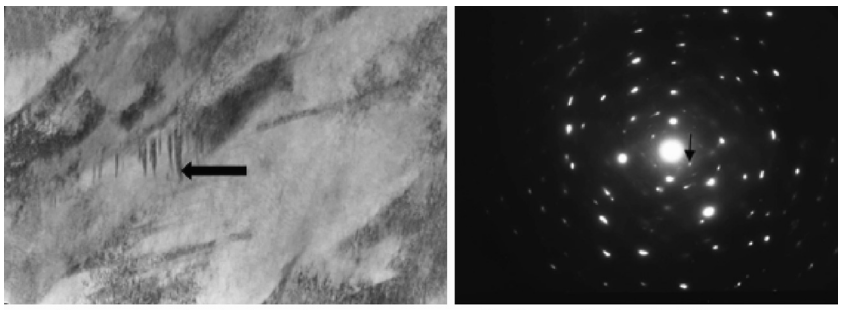

(a) Internally twinned stripes of martensite (depicted by arrow)

(b) Blurry reflections in diffraction pattern evidence a high density of defects in the microstructure. The arrow indicates the location shown in Fig.10(a)

**Fig. 10** Microstructure of the heat affected zone at a distance of 200 μm from the surface (TME, magnification 37,000×).

Fig. 10 shows the microstructure of this zone with visible stripes of martensite. Blurry reflections evidence a high density of defects in the microstructure of Fig. 10(b). The blurry diffraction pattern in Fig. 10 shows that martensite has a large number of twins and dislocation. Strongly deformed martensite indicates high thermal and structural stresses occurring during laser treatment of the material. The depth of the HAZ is about 520 μm. In turn, the raw material contains martensite and retained austenite. This microstructure was created during classical hardening and low tempering (see Fig. 11). Visible coniferous martensite with a small amount of retained austenite are found in Fig. 11(a). Non-metallic inclusions of irregular shape are revealed in the unprocessed material in Fig. 11(b). In order to identify the condition of the surface for the laser re-melted area and to compare it with that of the non-processed surface, a topography measurement was done. An optical, three-dimensional microscope based on focus-variation was used for this measurement. Measurement results are shown in Figs. 12–13. As it is apparent from these figures, laser re-melting caused an increase in the waviness of the treated surface with no noticeable deterioration of the surface roughness. Such an effect may be due to high compressive stresses in the surface layer after laser re-melting. The height difference between the top and bottom of the wave is about 24 μm. This height difference occurs over a length of about 600 μm. Described effects did not contribute to reducing the fatigue strength of the laser-processed drag strut.

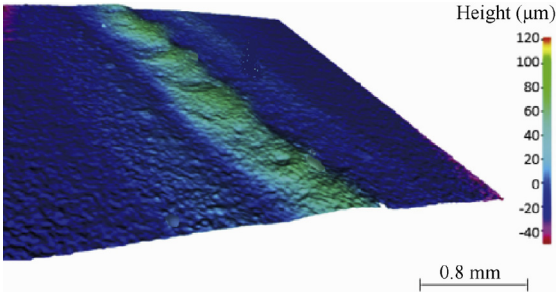


**Fig. 12** Changes in the topography of the surface due to laser treatment.

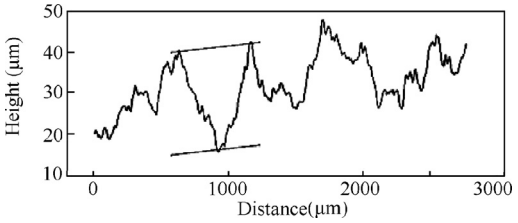


**Fig. 13** Surface profile in the axis of laser-melted paths.

During the fatigue test, the sleeve section of the drag strut was subjected to normal stresses ranging from −20 MPa to +203 MPa. Although laser surface re-melting has increased the roughness, it has not been found to initiate fatigue on

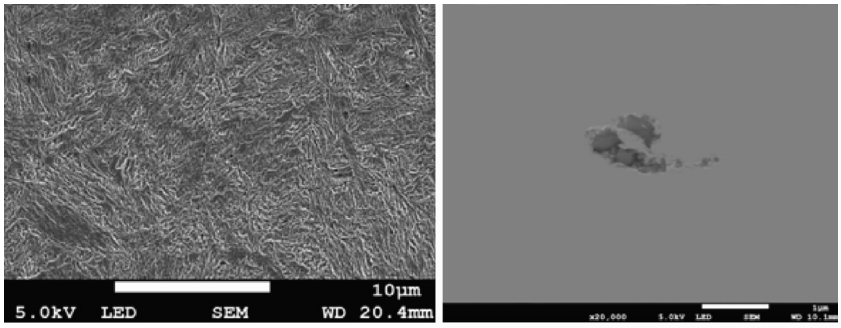


(a) Coniferous martensite with a small amount of retained austenite

(b) Non-metallic inclusions of irregular shape in the unprocessed material

**Fig. 11** Microstructure of the raw steel without laser treatment.

the treated surface. As shown by metallographic observations, only internal inclusion-initiated fatigue was observed. Because laser re-melting of steel resulted in dissolution of inclusions and reduced the amount of inclusions in the HAZ, there were much less cracks initiation sites in the HAZ than in the raw steel. The inclusions, on which fatigue cracks were initiated, were investigated through a scanning electron microscope (SEM) equipped with energy dispersive X-ray spectroscopy (EDS). Spot chemical composition was measured on the surface of inclusions, and it does not represent the content throughout the inclusions. Obtained results indicate that the inclusions are silicates, sulphides, and oxides. Table 7 presents the chemical compositions of the identified inclusions.

Metallographic observations have shown that fatigue initiated on inclusions in different ways depending on their shape, size, and mechanical properties. For example, the shape of sulphides was more or less close to a spherical or irregular shape with sharp edges. A shape of sulphides similar to an ellipse caused the initiation of fatigue (see Fig. 14(a)). In turn, spherical-shaped sulphides were a thin gap between the matrix and the inclusions (see Fig. 14(b)). It can be assumed that such a gap testifies that the inclusions were relatively weakly bonded to the matrix. A partially debonded inclusion and the associated residual stress state create a large stress gradient within the matrix which can lead to crack initiation at the location. Naragani et al.[34] using computer microtomography and far-field high-energy diffraction microscopy techniques, also reached similar conclusions. In turn, irregularly shaped sulphides with sharp edges are more detrimental than sulphides with smooth shapes when fatigue initiation is concerned. Fig. 14(c) shows a crack initiated inside a sulphide in the first stage and then developed in the metallic matrix. In some cases, cracks were developed only inside the sulphides in the direction perpendicular to the load axis, as shown in Fig. 14(d). Ma et al.[35] also reported that cyclic stress promoted 3D growth of pits associated with MnS inclusions, and the growth rates of pits in the direction perpendicular to the load axis were higher than those in the parallel direction.

Another reason for initiating fatigue cracks on non-metallic inclusions can be the strong differences in elastic properties between non-metallic inclusions and the surrounding metallic matrix. Lamagnere et al.[36] measured hardness and Young's modulus values of some of the non-metallic inclusions. According to their measurements, the hardness values of MnS and MnCaS sulfides fall within a range from 3.2 to 3.4

**Table 7** Chemical compositions on inclusion surfaces in weight (unit: %).

| Inclusion | Type I | Type II | Type III |
|---|---|---|---|
| Al | 11.88 | | 5.22 |
| Ca | 0.25 | 2.40 | 1.68 |
| Si | 0.61 | 0.33 | 17.39 |
| Mg | 6.70 | 2.21 | 4.35 |
| O | 19.59 | | 42.65 |
| S | 0.11 | 32.08 | 0.35 |
| Mn | 0.86 | 44.13 | 0.36 |
| Fe | Total | Total | Total |

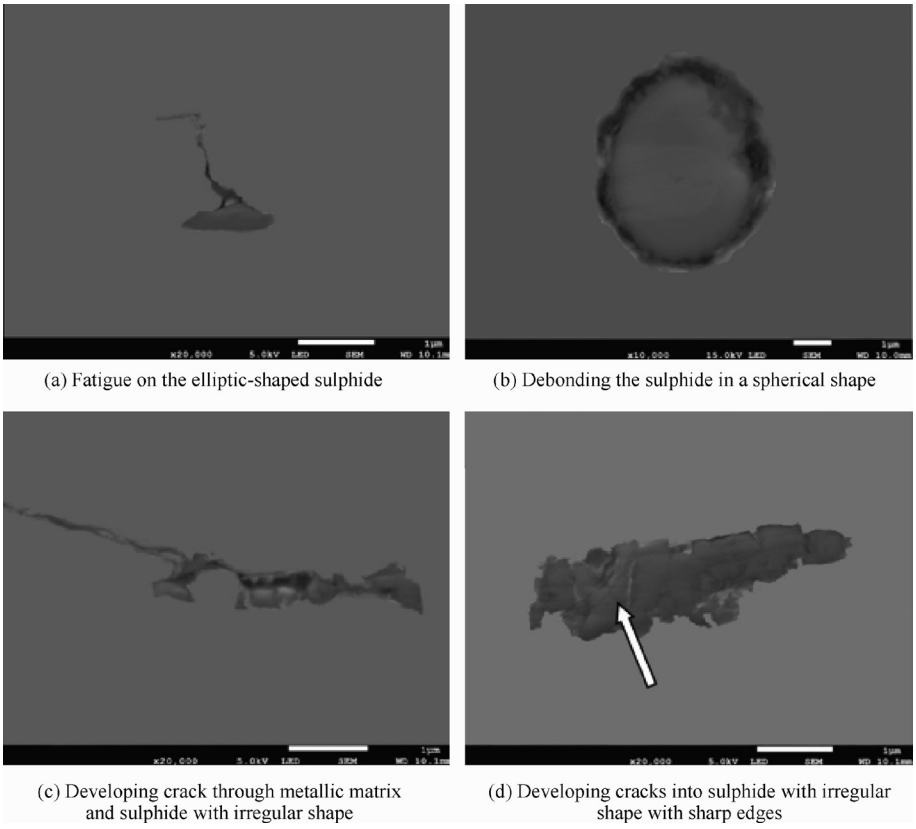

(a) Fatigue on the elliptic-shaped sulphide

(b) Debonding the sulphide in a spherical shape

(c) Developing crack through metallic matrix and sulphide with irregular shape

(d) Developing cracks into sulphide with irregular shape with sharp edges

**Fig. 14** Initiating fatigue cracks on the sulphides.

GPa which are significantly lower than that of the matrix after laser treatment. For this reason, cracks were primarily initiated on sulphides. The hardness values of aluminium oxide $Al_2O_3$, spinel $(Al_2O_3)_3$ (MgO), calcium aluminate $(AI_2O_3)_6$(CaO), and calcium aluminate $(Al_2O_3)_2$(CaO) are 32.2 GPa, 26.6 GPa, 18.2 GPa, and 9.6 GPa, respectively, which are significantly higher than that of the matrix before laser re-melting. Laser re-melting of the steel significantly increases the hardness and elastic properties of the metallic matrix (see below) and thus contributes to reducing the difference between the properties of the matrix and oxides or spinels. Fig. 15(a) shows an oxide deposited on a sulphide. As shown in Fig. 15(a), partial separation between the oxide and the sulphide occurred under cyclic loading due to a greater difference in hardness between the oxide and the sulphide than between the oxide and the matrix. Some researchers[37,38] reported that brittle inclusions with Young's modulus greater than that of the matrix, e.g., $Al_2O_3$, are regarded as more harmful than soft inclusions, such as sulphides, and they favour crack initiation under cyclic loading at room temperature. In their experiment, the authors did not observe initiation of cracks on hard oxide and silicate inclusions (see Fig. 15(b)–(c)). In the presence of hard oxides and silicates, the dimensions of seat inclusions were larger than those of embedded inclusions, without visible cracks in neither the matrix nor inclusions. Probably, after the debonding between the matrix and inclusions, friction wear of the softer matrix occurred. Hong et al.[39] reported that the mechanism of crack initiation and early growth for very-high-cycle fatigue (VHCF) is basically different from those for low-cycle fatigue (LCF) and high-cycle fatigue (HCF).

For high-strength steels as an instance, the process of VHCF is commonly caused by subsurface or interior crack initiation. The crack origin, surrounding an inclusion or another defect, contains a rough region of fine-granular-area (FGA). FGA is regarded as the characteristic region of crack initiation for VHCF.[39] Moreover, many other researchers have described the FGA region for VHCF.[40–43] FGA was also observed in our investigation, although the experiment concerned HCF. At the bottom of empty cavities, metallographic observations revealed regions of FGA which are a characteristic for VHCF (see Fig. 15(d)). Such a wide variety of mechanisms of fatigue crack initiation cannot be explained solely by the shape, size, and properties of the inclusions. In the processed alloy, laser re-melting has generated residual stresses of different values depending on the location of the material relative to the re-melted paths.

Since the initiation of fatigue cracks in the sleeve of the drag strut was slower than in the welded joint connecting the sleeve and the eyelet, it can be assumed that in the laser-treated sleeve, there were residual stresses which were slowing down the initiation of fatigue cracks. In addition, the laser treatment changed the mechanical properties of the workpiece, which could also contribute to slowing the initiation of fatigue cracks. To determine the effects of these two factors, hardness tests were performed using a nanoindenter. Hardness profiles and changes of elastic properties of the laser-treated material as well as the raw material at a distance of 0.5 mm from the boundary of the heat-affected zone are shown in Fig. 16, in which hardness was increased in all analyzed areas. The greatest increase in hardness was observed for the melted material. This effect could be attributed to the high refinement of the

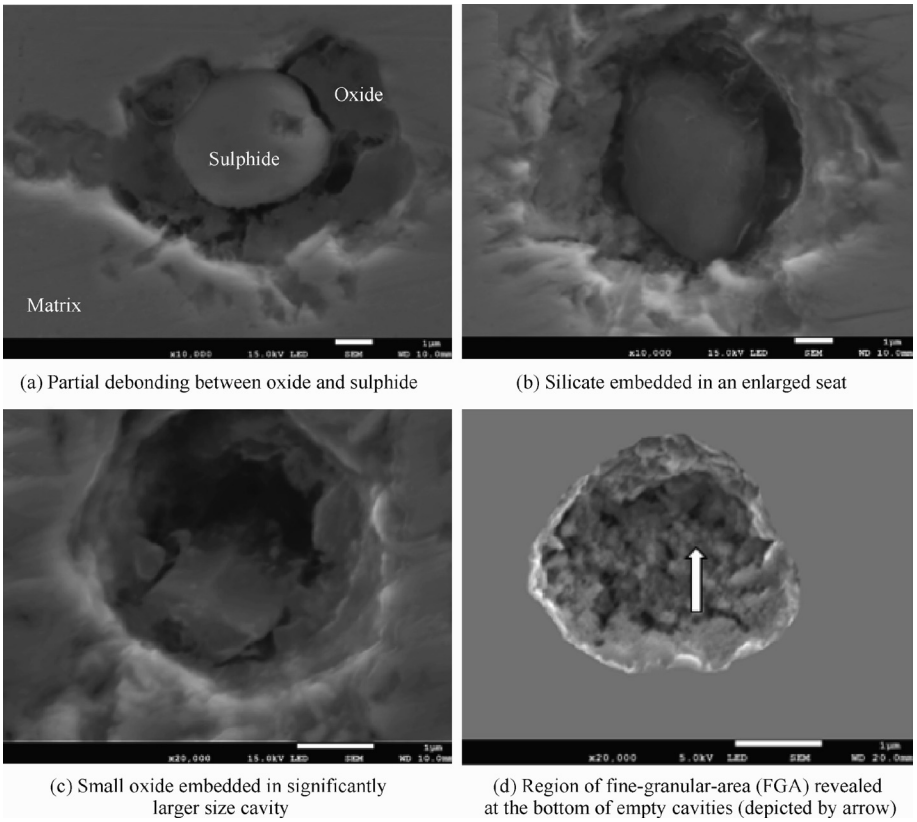


(a) Partial debonding between oxide and sulphide

(b) Silicate embedded in an enlarged seat

(c) Small oxide embedded in significantly larger size cavity

(d) Region of fine-granular-area (FGA) revealed at the bottom of empty cavities (depicted by arrow)

**Fig. 15** Initiating fatigue cracks on ceramic inclusions.

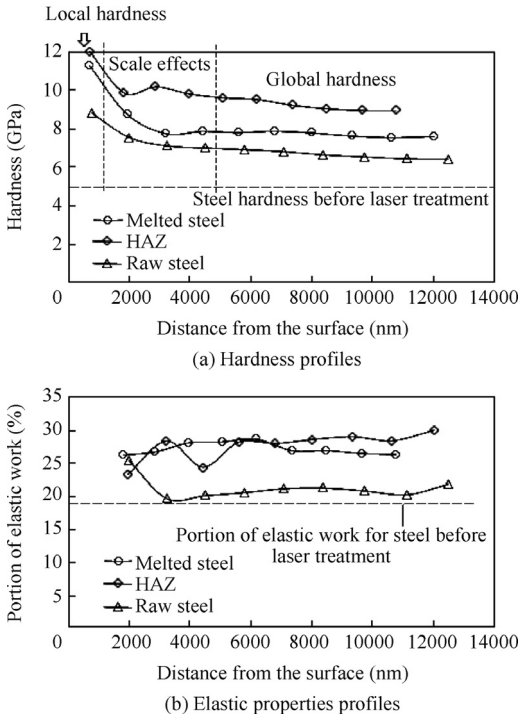


**Fig. 16** Mechanical properties of the laser-processed undercarriage drag strut.

microstructure of the melted material resulting in an increase in the density of defects in the crystalline lattice and thus an increase in the strength properties of the alloy. The second reason that contributed to increased hardness was the scale effect. Hardness profiles were determined in a multiple-load cycle. The minimum load was 100 mN, and the maximum load was 20 times higher and amounted to 20 N. For small loads, local hardness was measured, while for higher loads, global hardness was obtained (see Fig. 16(a)). Hardness tests also allowed the determination of the elastic properties of the processed material. During the hardness tests, plastic and elastic works of deformation of the tested material were measured. The portion of elastic work, $W_{el}$, was defined as the area under the unload curve in the diagram of load vs. indenter displacement. Fig. 16(b) shows changes of portion of elastic work (related to the total work of deformation during indentation) for three analyzed areas. As can be seen in Fig. 16(b), the elastic properties of both the melted area and the HAZ have increased as a result of laser treatment.

The increases in the elastic properties in these areas were similar and amounted to about 60% of the initial values. Hardness measurements were made again after annealing (see Fig. 17). Such an approach allowed the determination of residual stresses in processed areas. Fig. 18 shows the residual stresses calculated from Fig. 17 as $\sigma = \Delta P/A$, where $\Delta P$ is the difference in loads resulting in the same displacement of the indenter before and after annealing and $A$ is the surface contact of the indentation. As shown in Fig. 18, the highest compressive stresses occur in the HAZ. They reach a value of 2.5 GPa. In the areas of the melted material, there are lower compressive stresses than in the HAZ. Their values range from 0 to 700 MPa. In the raw material at a distance of 0.5 mm from the HAZ, there are tensile stresses, the values of which range from

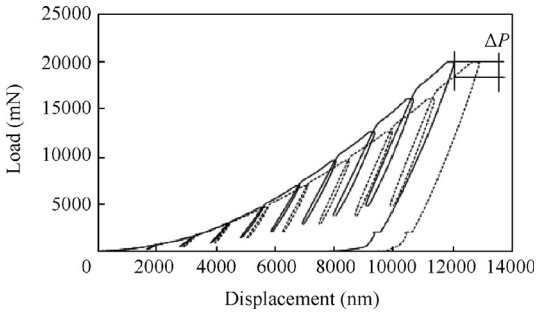


**Fig. 17** Load and unload curves obtained in a multiple-load cycle with an increasing load in the range from 100 mN to 20 N for the melted area before stress relief annealing (solid line) and after stress relief annealing (dashed line).

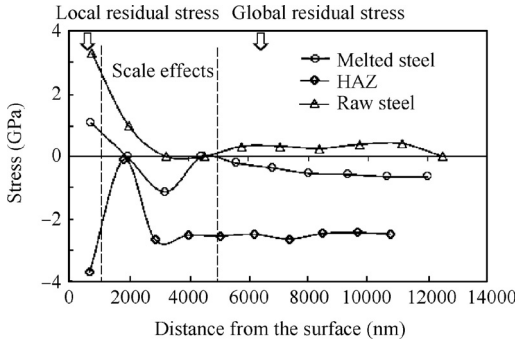


**Fig. 18** Residual stress profiles for analyzed areas.

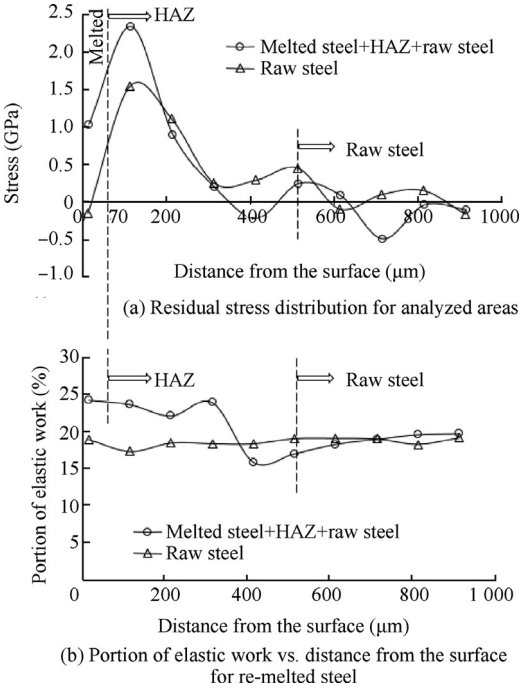


**Fig. 19** Residual stresses and elastic properties measured on the cross section.

0 to 350 MPa. In order to calculate residual stresses at greater distances from the surface, similar hardness tests were performed on the cross section.

Fig. 19(a) shows residual stress distributions in the range of 15–915 μm from the surface, and Fig. 19(b) shows distributions of portion of elastic work. As is apparent from Fig. 19(a), the residual stress changes from compressive to tensile in zone II in the melted material. At a distance of 70 μm from the surface, the melted zone passes into the HAZ, and the stress oscillates from tensiling to compressing. Residual stresses of the raw material pass from tensile to compressive, similar to that in the HAZ. In turn, the portions of elastic work in the melted zone and the HAZ at a distance of 315 μm from the surface are still high and about 25%. Only at a distance greater than 315 μm from the surface, the elastic properties reaches the same values as those of the raw materials before the laser treatment. Due to the fact that the process of fatigue was caused by interior crack initiation, it can be assumed that the residual stresses on the surface and in the subsurface layers have delayed the initiation of fatigue cracks. In the re-melted steel and the HAZ, there were high compressive residual stresses in the surface and subsurface layers, which inhibited the initiation of fatigue in these areas. According to the linear elastic fracture mechanics superposition concept, the total stress intensity factor value consists of the part due to the applied external load and the part due to residual stresses. If the resid-

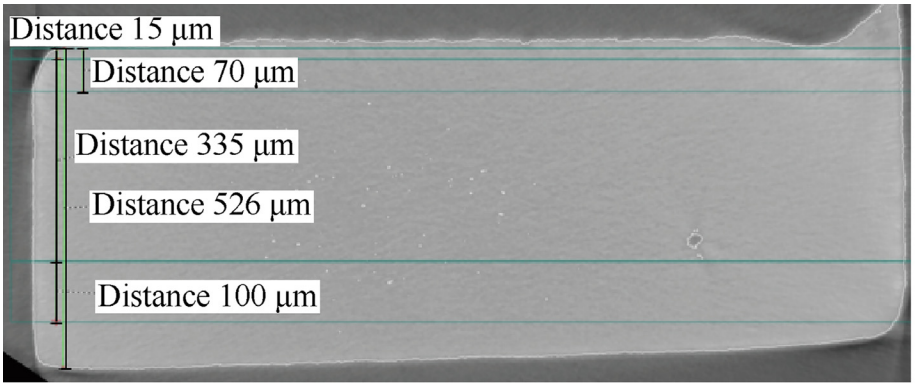


(a) CT scan of the sample with marked areas for detection of fatigue crack initiation sites

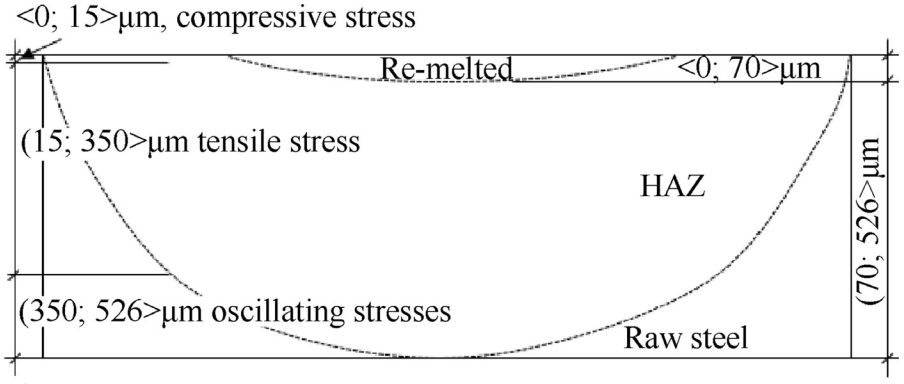


(b) A sample scheme with marked areas of different nature of residual stresses and microstructure

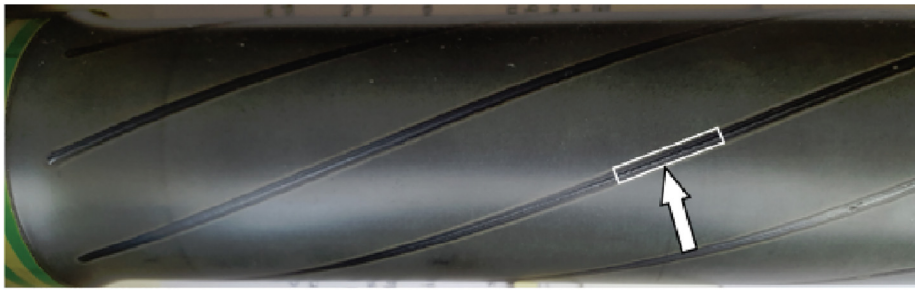

(c) Place of sample cutout for testing-depicted by arrow the sample size 0.526 mm×2 mm×14.64 m

**Fig. 20** Sample for CT testing.

ual stresses originate from a compressive stress, they reduce the total stress intensity at the crack tip and thus reduce the rate of crack propagation. In addition, the residual stresses influence the strain and dislocation density in the vicinity of inclusions, thus the mechanism of the development of fatigue crack nucleation. The mechanism of fatigue crack nucleation involves slip accumulation and localization, the establishment of local, high geometrically necessary dislocations densities, and consequent local stress, giving rise to both non-metallic inclusion cracking and inclusion/matrix decohesion.

In order to determine the effects of the microstructure of steel and the residual stress on the rate of initiation of fatigue cracks, a sample was scanned using a computer microtomograph. Fig. 20 presents the sample used for the study with the marked areas for detection of fatigue cracking initiation sites. To determine the content of defects in alloy subjected to laser treatment, four volumes of metal were extracted in the scanned sample. The volumes of material in which fatigue crack initiation sites were searched corresponded to the nature of the residual stresses in those volumes or the type of microstructure of the material. Figs. 21 and 22 show the results of these analyzes (MZ I – melted "zone I", MZ II – melted "zone II", RM – raw material, and HAZ – heat affected zone). As shown in Figs. 21 and 22, the lowest number of defects are in the volume of material extracted from a depth of 0–15 μm. In this volume of material, there are high compressive residual stresses. The microstructure of this volume of material is partly as in "zone I" (about 30%) of the re-melted material and partly as in the HAZ (about 70%). In turn, the greatest number of defects due to fatigue occur for the volume of the re-melted steel extracted from a depth of 15–350 μm. The microstructure of this volume of material consists of about 2% of the microstructure of the melted material such as in "zone II", 90% of the microstructure such as in the HAZ,

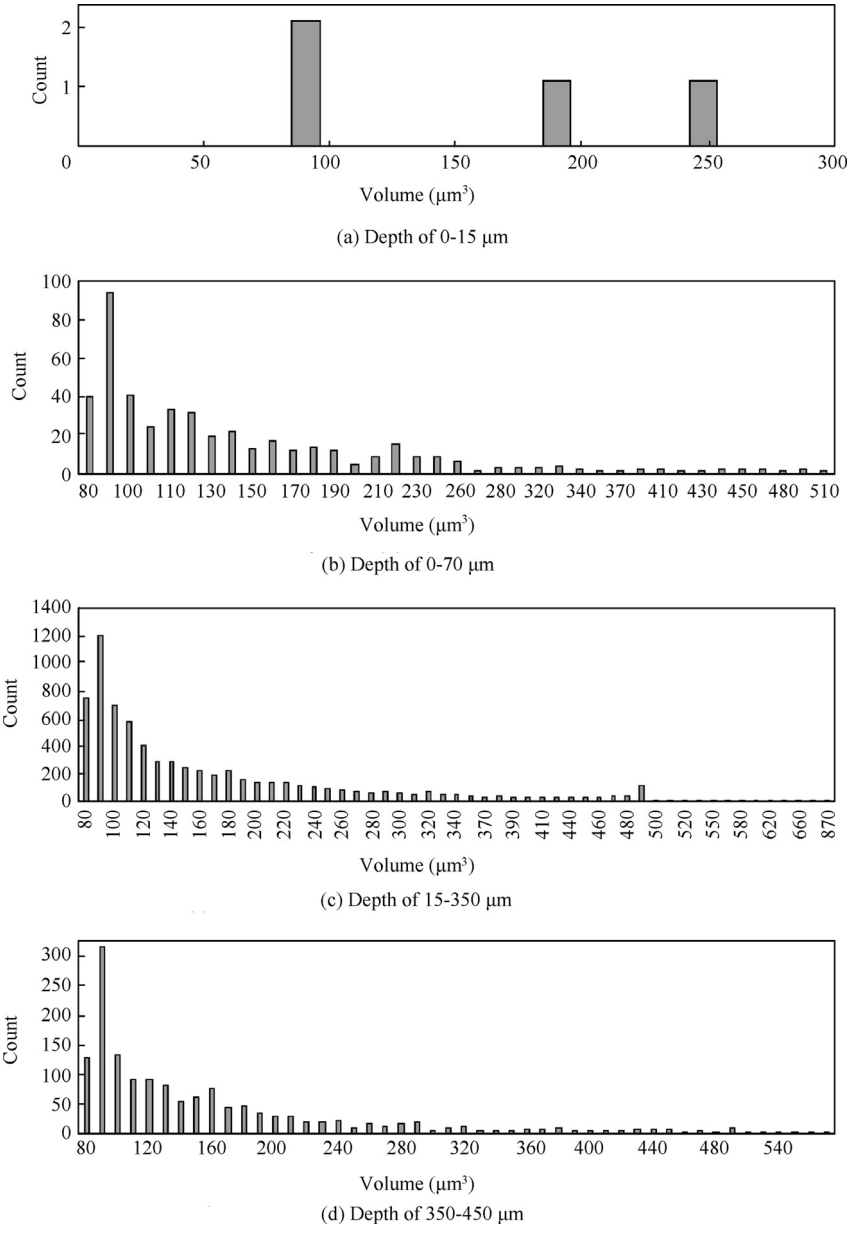


**Fig. 21** Histograms showing the number and size of defects (fatigue crack initiation sites).

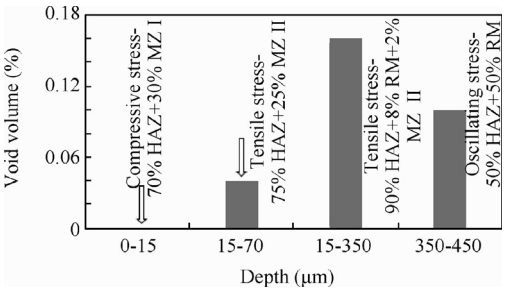


**Fig. 22** Percentage share of defects caused by fatigue (relative to the volume of the analyzed material) for various volumes of material being extracted.

and 8% of the microstructure such as in the raw material. The characteristic feature of this volume of material is the presence of high tensile residual stresses in it. A slightly lower number of defects are in the volume of material that has a microstructure such as in the HAZ (about 50%) and one in the raw steel (about 50%), but the residual stresses are both compressive and tensile stresses. Such a case occurs for the volume of material extracted from a depth of 350–450 μm. Even fewer defects have the volume extracted from a depth of 15–70 mm, despite the tensile residual stresses therein. The microstructure of this volume consists of about 25% of the microstructure of the melted material such as in "zone II" and 75% of the microstructure such as in the HAZ. In all analyzed volumes of material, there was a predominant proportion of microstructure such as that found in the HAZ. In the volume of material with the lowest number of defects, the share of this microstructure was 70%, and in the volume with the highest number of defects, this share was 90%. It can be assumed that the HAZ microstructure, although it increases the hardness and elastic properties of the material, is not decisive for increasing the fatigue resistance of the material. In volumes of material with the lowest number of fatigue failures, a significant volume share has a melted microstructure. It can therefore be assumed that it has a positive effect on the fatigue resistance. This type of microstructures slows down the rate of fatigue crack initiation even if the material has a high tensile residual stress.

Because the cellular/dendritic microstructure in the re-melted areas is strongly refined; therefore, according to the Hall-Pitch effect, the yield strength of the alloy increases. In turn, the increase in the yield strength of the alloy results in a reduction of the zone of plastic deformation of the metallic matrix in front of the fatigue crack. A smaller area of the plasticized material reduces the propagation rate of a fatigue crack. A higher yield strength of the steel due to refinement of its microstructure also affects the nucleation of fatigue cracks. The higher the yield strength of the material is, the larger loads are required to produce extrusions and intrusions necessary to initiate fatigue cracking.

## 4. Conclusions

The main part of a drag strut used in an aircraft landing gear was re-melted using a $CO_2$ laser beam. Eight re-melted paths were made in the form of spiral lines along the axis of the drag strut. The re-melted drag strut was then subjected to a fatigue test, and fatigue test results were compared with those of a drag strut which was not subjected to laser treatment. It has been shown that both residual compressive stresses and the microstructure of the re-melted zones contribute to an increased resistance to fatigue wear. Both the ultra-fine cellular structure and the dendritic structure with dendrites perpendicular to the fatigue stresses direction are advantageous in terms of the fatigue resistance of the re-melt alloy. This type of microstructure has a higher hardness and better elastic properties than those of a microstructure after conventional hardening and tempering, which results in both a delayed initiation of fatigue cracks and a reduction in the propagation rate of fatigue cracks. Additionally, the compressive stress generated during laser re-melting also contributes to an increase of the fatigue resistance of the material. The obtained results allow forming the following conclusions:

(1) The fatigue test showed that the drag strut was able to withstand 1700 simulated cycles of landing. This result was 70% better than that obtained for a drag strut with no laser treatment.
(2) Laser re-melting improved the hardness and elastic properties of the metal matrix, and thus increased the differences between the properties of the metal matrix and sulphides and decreased the differences between the properties of the metal matrix and silicates as well as oxides. As a result, fatigue cracks were initiated on sulphides.
(3) The investigations of the number of fatigue crack initiation sites indicated that the zone of the re-melted material containing a microstructure composed of martensite and retained austenite with both the ultra-fine cellular structure and the dendritic structure contributed to a delayed initiation of fatigue cracks.
(4) Laser re-melting caused a generation of suitable compressive residual stresses in the re-melted material and the HAZ to a depth of up to 15 μm. In such a distance from the surface, residual stresses in the re-melted material reached a value of 750 MPa, and in the HAZ, a value of 2.5 GPa. At the same time in the raw material at these depths, there are tensile residual stresses of 350 MPa.
(5) Laser re-melting of the steel leads to an increased waviness with a slight change in the surface roughness. This effect does not contribute to reducing the fatigue life of the processed drag strut.

## References

1. Giren BG, Szkodo M. Cavitation erosion of some alloys manufactured on steel and iron surfaces by laser beam. *J Mater Eng Perform* 2003;**12**(5):512–20.
2. Giren BG, Szkodo M, Cenian A. Cavitation resistance of 45 and 2Cr13 steels enriched with laser deposited Hf, SiC or SiC + AlNi powders. In: Wolinski W, Jankiewicz Z, editors. *Laser Technology VI: Applications*. 2000;142–8.
3. Ge M-Z, Xiang J-Y. Effect of laser shock peening on microstructure and fatigue crack growth rate of AZ31B magnesium alloy. *J Alloy Compd* 2016;**680**:544–52.
4. Prabhakaran S, Kalainathan S. Warm laser shock peening without coating induced phase transformations and pinning effect on fatigue life of low-alloy steel. *Mater Des* 2016;**107**:98–107.
5. Prabhakaran S, Kalainathan S. Compound technology of manufacturing and multiple laser peening on microstructure and fatigue life of dual-phase spring steel. *Mater Sci Eng, A* 2016;**674**:634–45.

6. Tekeli S. Enhancement of fatigue strength of SAE 9245 steel by shot peening. *Mater Lett* 2002;**57**(3):604–8.
7. Benedetti M, Fontanari V, Allahkarami M, Hanan JC, Bandini M. On the combination of the critical distance theory with a multiaxial fatigue criterion for predicting the fatigue strength of notched and plain shot-peened parts. *Int J Fatigue* 2016;**93**(Part 1):133–47.
8. Carvalho SM, Baptista CARP, Lima MSF. Fatigue in laser welded titanium tubes intended for use in aircraft pneumatic systems. *Int J Fatigue* 2016;**90**:47–56.
9. Reitemeyer D, Schultz V, Syassen F, Seefeld T, Vollertsen F. Laser welding of large scale stainless steel aircraft structures. *Phys Procedia* 2013;**41**:106–11.
10. Vasu A, Gobal K, Grandhi RV. A computational methodology for determining the optimum re-peening schedule to increase the fatigue life of laser peened aircraft components. *Int J Fatigue* 2015;**70**:395–405.
11. Dittrich D, Standfuss J, Liebscher J, Brenner B, Beyer E. Laser beam welding of hard to weld Al alloys for a regional aircraft fuselage design – first results. *Phys Procedia* 2011;**12**(Part A):113–22.
12. Schnubel D, Horstmann M, Ventzke V, Riekehr S, Staron P, Fischer T, et al. Retardation of fatigue crack growth in aircraft aluminium alloys via laser heating – Experimental proof of concept. *Mater Sci Eng, A* 2012;**546**:8–14.
13. Leap MJ, Rankin J, Harrison J, Hackel L, Nemeth J, Candela J. Effects of laser peening on fatigue life in an arrestment hook shank application for Naval aircraft. *Int J Fatigue* 2011;**33**(6):788–99.
14. Zhang X, Li H, Duan S, Yu XL, Feng JY, Wang B, et al. Modeling of residual stress field induced in Ti–6Al–4V alloy plate by two sided laser shock processing. *Surf Coat Technol* 2015;**280**:163–73.
15. Liverani E, Lutey AHA, Ascari A, Fortunato A, Tomesani L. A complete residual stress model for laser surface hardening of complex medium carbon steel components. *Surf Coat Technol* 2016;**302**:100–6.
16. Umapathi A, Swaroop S. Residual stress distribution in a laser peened Ti-2.5Cu alloy. *Surf Coat Technol* 2016;**307**(Part A): 38–46.
17. Su R, Liu H, Liang Y, Yu F. Residual thermal stress of a mounted KDP crystal after cooling and its effects on second harmonic generation of a high-average-power laser. *Opt Laser Technol* 2017;**87**:43–50.
18. Maawad E, Gan W, Hofmann M, Ventzke V, Riekehr S, Brokmeier H-G, et al. Influence of crystallographic texture on the microstructure, tensile properties and residual stress state of laser-welded titanium joints. *Mater Des* 2016;**101**:137–45.
19. Oliveira JP, Fernandes FMB, Miranda RM, Schell N, Ocaña JL. Residual stress analysis in laser welded NiTi sheets using synchrotron X-ray diffraction. *Mater Des* 2016;**100**:180–7.
20. Karthik D, Swaroop S. Laser peening without coating induced phase transformation and thermal relaxation of residual stresses in AISI 321 steel. *Surf Coat Technol* 2016;**291**:161–71.
21. Salimianrizi A, Foroozmehr E, Badrossamay M, Farrokhpour H. Effect of laser shock peening on surface properties and residual stress of Al6061-T6. *Opt Lasers Eng* 2016;**77**:112–7.
22. Qiao H, Zhao J, Zhang G, Gao Y. Effects of laser shock peening on microstructure and residual stress evolution in Ti–45Al–2Cr–2Nb–0.2B alloy. *Surf Coat Technol* 2015;**276**:145–51.
23. Bień A, Szkodo M. Surface treatment of C80U steel by long $CO_2$ laser pulses. *J Mater Process Technol* 2015;**217**:114–21.
24. Grum J, Slabe JM. Effect of laser-remelting of surface cracks on microstructure and residual stresses in 12Ni maraging steel. *Appl Surf Sci* 2006;**252**(13):4486–92.
25. Yang W, Zhou T, Zhang W, Li J, Chen ZK, Chang F, et al. Effect of one-step laser processed biomimetic coupling units' degrees on rolling contact fatigue wear resistance of train track alloy steel. *Surf Coat Technol* 2015;**277**:181–7.
26. Gerritsen C, Vanrostenberghe S, Doré M. Diode laser weld toe re-melting as a means of fatigue strength improvement in high strength steels. *Procedia Eng* 2013;**66**:171–80.
27. Lavvafi H, Lewandowski ME, Schwam D, Lewandowski JJ. Effects of surface laser treatments on microstructure, tension, and fatigue behavior of AISI 316LVM biomedical wires. *Mater Sci Eng, A* 2017;**688**:101–13.
28. Szkodo M, Bien A. Influence of laser processing of the low alloy medium carbon structural steel on the development of the fatigue crack. *Surf Coat Technol* 2016;**296**:117–23.
29. Bień A, Kłysz S. Method to block the propagation of fatigue cracks (in Polish). Poland, 2012.
30. Bień A. Laser surface modification of metal alloys and its effect on the fatigue crack propagation in terms of the microstructure (in Polish). UWM, 2013.
31. Breczko T, Bien A. Influence of multiple melting on the structure and geometry of the surface layer of 50H steel. *Proc SPIE* 2006;**6253**, 62530E–7.
32. Teng C, Pal D, Gong HJ, Zeng K, Briggs K, Patil N, et al. A review of defect modeling in laser material processing. *Addit Manuf* 2017;**14**:137–47.
33. Lee Y-H, Dongil K. Residual stresses in DLC/Si and Au/Si systems: application of a stress relaxation model to the nanoindentation technique. *J Mater Res* 2002;**17**(4):901–6.
34. Naragani D, Sangid MD, Shade PA, Schuren JC, Sharma H, Park J-S, et al. Investigation of fatigue crack initiation from a non-metallic inclusion via high energy X-ray diffraction microscopy. *Acta Mater* 2017;**137**:71–84.
35. Ma J, Zhang B, Wang J, Wang G, Han EH, Ke W. Anisotropic 3D growth of corrosion pits initiated at MnS inclusions for A537 steel during corrosion fatigue. *Corros Sci* 2010;**52**(9):2867–77.
36. Lamagnere P, Girodin D, Meynaud P, Vergne F, Vincent A. Study of elasto-plastic properties of microheterogeneities by means of nano-indentation measurements: application to bearing steels. *Mater Sci Eng, A* 1996;**215**(1–2):134–42.
37. Alfredsson B, Olsson E. Multi-axial fatigue initiation at inclusions and subsequent crack growth in a bainitic high strength roller bearing steel at uniaxial experiments. *Int J Fatigue* 2012;**41**:130–9.
38. Texier D, Cormier J, Villechaise P, Stinville J-C, Torbet CJ, Pierret S, et al. Crack initiation sensitivity of wrought direct aged alloy 718 in the very high cycle fatigue regime: the role of non-metallic inclusions. *Mater Sci Eng, A* 2016;**678**:122–36.
39. Hong Y, Liu X, Lei Z, Sun C. The formation mechanism of characteristic region at crack initiation for very-high-cycle fatigue of high-strength steels. *Int J Fatigue* 2016;**89**:108–18.
40. Abdesselam H, Crepin J, Pineau A, Rouffie AL, Menut-Yournadre L, Morgeneyer TF. On the crystallographic, stage I-like, character of fine granular area formation in internal fish-eye fatigue cracks. *Int J Fatigue* 2018;**106**:132–42.
41. Tofique MW, Bergström J, Svensson K. Very high cycle fatigue of cold rolled stainless steels, crack initiation and formation of the fine granular area. *Int J Fatigue* 2017;**100**(1):238–50.
42. Li YD, Zhang LL, Fei YH, Liu XY, Li MX. On the formation mechanisms of fine granular area (FGA) on the fracture surface for high strength steels in the VHCF regime. *Int J Fatigue* 2016;**82** (3):402–10.
43. Sakai T, Nakagawa A, Oguma N, Nakamura Y, Ueno A, Kikuchi S. A review on fatigue fracture modes of structural metallic materials in very high cycle regime. *Int J Fatigue* 2016;**93** (2):339–51.